Research Article Vol. 64, No. 26 / 10 September 2025 / Applied Optics 7645

applied optics

Polarization-independent and rotationally symmetric $LiNbO_3$ tetramer metasurface supported by bound states in the continuum

Jianing Shi,[1] Jingwei Lv,[1,*] Yanru Ren,[1] Liangliang Li,[1] Renfeng Li,[1] Weijie Kong,[1] Qiang Liu,[1] Jianxin Wang,[1] Wei Liu,[1] Paul K. Chu,[2,3,4] Chao Liu,[1] and Haihao Fu

[1]School of Physics and Electronic Engineering, Northeast Petroleum University, Daqing 163318, China
[2]Department of Physics, City University of Hong Kong, Tat Chee Avenue, Kowloon, Hong Kong SAR, China
[3]Department of Materials Science and Engineering, City University of Hong Kong, Tat Chee Avenue, Kowloon, Hong Kong SAR, China
[4]Department of Biomedical Engineering, City University of Hong Kong, Tat Chee Avenue, Kowloon, Hong Kong SAR, China
*lvjingwei2009123@126.com

Received 6 June 2025; revised 26 July 2025; accepted 14 August 2025; posted 15 August 2025; published 29 August 2025

Metasurface transmission, where light of different wavelengths or modes is redistributed and regulated by the metasurface structure, plays a crucial role in modern photonics and nano-optics research. Herein, an in-plane symmetry-breaking approach is designed to excite quadruple transmission dips using the $LiNbO_3$ metasurface based on the leaked plasmonic bound states in the continuum (BIC). The influence of the difference between the major and minor diameters of the ellipse of the $LiNbO_3$ metasurface is accounted for, and the C_{4v} symmetry is maintained. According to the theoretical derivation, four quasi-BICs are obtained, with the highest quality factor (Q-factor) reaching 2.1×10^4 and the figure of merit being 5707 RIU^{-1}. The multi-level decomposition and near-field analysis of the four specific BIC modes indicate that the modes are excited by toroidal dipoles and magnetic quadrupoles rather than any related guided-mode resonances. The results reveal that the four resonances are polarization-independent, and their properties are maintained even for circularly polarized light. The results provide insights into the utilization of $LiNbO_3$ in advanced integrated nonlinear optics for integrated optics, biosensing, filtering, and lasers.

https://doi.org/10.1364/AO.569976

1. INTRODUCTION

Different metasurfaces utilizing transmission-based bound states in the continuum (BIC) have been proposed and analyzed, with applications ranging from highly efficient optical filters and sensor devices to laser cavities and enhanced light–matter interaction systems. Researchers have theoretically verified and developed a number of metasurface devices, including superlenses [1], invisibility cloaks [2], filters [3], imaging polarimeters [4], and sensors [5]. Specifically, resonant periodic nanostructures composed of different materials have distinct optical and sensing properties [6]. Metallic nanoparticles capable of exciting surface plasmon resonance enhance the near-field confinement and provide strong optical confinement at subwavelength scales [7]. However, the inherent ohmic losses when metals convert energy restrict the sensitivity in optical sensor systems [8]. Hence, metasurfaces made of high refractive index dielectric materials have been proposed because of their large nonlinear coefficients [9]. Similar to metallic nanostructures that support plasmonic resonances, they provide multipolar electric and magnetic resonances known as Mie resonances [10]. The moderate quality factor (Q-factor) of Mie resonance is always accompanied by moderate electric field confinement, thereby limiting the light–matter coupling strength [11–13]. These attributes render them an exemplary platform for sensing [14] and surface-enhanced spectroscopy [15].

The Q-factor of resonance is defined as the energy dissipation in each cycle of oscillation versus the energy stored in the resonator [16]. A higher Q-factor is expected to produce stronger field confinement in the resonator [17] to boost light–matter interactions for applications such as surface-emitting lasing [18], biomedical sensors [19], and nonlinear frequency converters [20]. Fortunately, BIC can provide a feasible solution to realize an almost infinite Q-factor. BIC is a type of electromagnetic eigenstate that coexists in the continuous spectrum but is completely confined within a resonant system without radiating energy [21]. Ideal BICs exist in lossless or extreme structures with zero linewidth and infinite Q-factor. It can turn into the quasi-BIC (QBIC) by introducing a finite coupling to the radiation continuum, resulting in an ultrahigh Q-factor and an observable resonance in far-field spectra [22].

Recently, there has been a rapid advance in materials science and optical technology, leading to innovations in optical devices, sensors, and information processing technology. Xi *et al.* [22] have proposed a multifunctional switchable metamaterial device. By controlling two phase-change materials, graphene and vanadium dioxide (VO_2), the conversion and regulation of BIC and absorber are achieved. However, there is room for improvement with regard to biosensing capability. Fan *et al.* [23] have designed a graphene–metal boat structure with a metal mirror. It has dual-quasi BICs and a maximum sensitivity of 860 nm RIU^{-1}. In spite of its good properties, it is complicated to prepare. In order to improve transmission, Gao *et al.* [24] have proposed subwavelength nanograting metasurfaces fabricated in a crystalline lithium niobate film. They can tune the spectral response by simply varying the geometric parameters. However, the FWHM of the transmission spectrum of the metasurfaces is too large, consequently causing overlapping of different transmissions and making it difficult to distinguish them accurately. Kanyang *et al.* [25] have proposed an $LiNbO_3$ metasurface using nanorods to connect elliptical columns for effective separation of transmissions and reduced FWHM. However, precise control of the position of nanorods and ellipses is required, making the actual production difficult. In order to reduce the difficulty of manufacturing, He *et al.* [26] have prepared a metasurface composed of single-sided cutting with specific corner radii, showing a narrower FWHM and reduced operational requirements during preparation. However, it still requires strict control of the incident light direction. In summary, the design and fabrication of a metasurface with a narrow FWHM, simple structure, and polarization independence remain a formidable challenge.

In this work, a windmill elliptic tetramer metasurface (WETM) with fourfold rotational symmetry is presented. The structure comprises four $LiNbO_3$ ellipsoidal columns arranged on an SiO_2 substrate. The four QBIC resonances are excited by varying the unilateral radius of the ellipsoids of the metasurface consisting of a periodic array of nanostructures. Multipole decomposition calculations and field analyses are performed. The resonances primarily arise from the toroidal dipole and magnetic quadrupole modes. The QBIC mode delivers remarkable performance, such as a maximum sensitivity (S) of 753.33 GHz/RIU and a figure of merit (FOM) of 5707 RIU^{-1}. The $LiNbO_3$ metasurface, boasting high sensitivity, a simple structure, polarization independence, and rotational symmetry, has large potential in optical sensors, lasers, optical modulators, and nonlinear optical devices.

2. MODEL AND METHOD

In order to simplify the metasurface dielectric structure and to make it practical for fabrication, the structure of WETM is designed and shown in Figs. 1(a)–1(c). The unit cell consists of a periodic array of four $LiNbO_3$ ellipsoidal columns arranged on an SiO_2 substrate, as shown in Fig. 1(b). $LiNbO_3$ is selected for the ellipsoidal columns tetramers because it is highly transparent in the near-infrared and near-ultraviolet spectral regions. Moreover, the tetramer structure enhances light–matter interactions and has high surface sensitivity. The nanopillars have the same heights ($\mathbf{h1} = 450$ nm) and radii ($\mathbf{r} = 250$ nm)

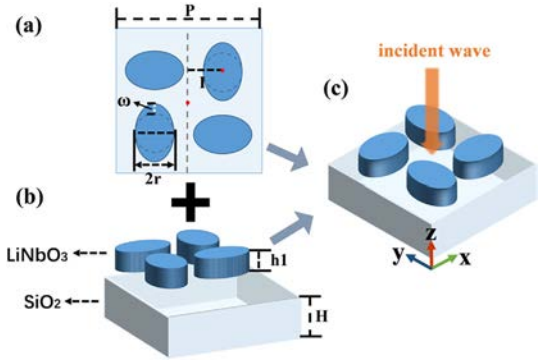

Fig. 1. (a) Metasurface unit cell with a detailed 2D geometric description; (b) a schematic of the $LiNbO_3$ ellipsoidal column metasurface arranged on an SiO_2 substrate; (c) a unit of the WETM.

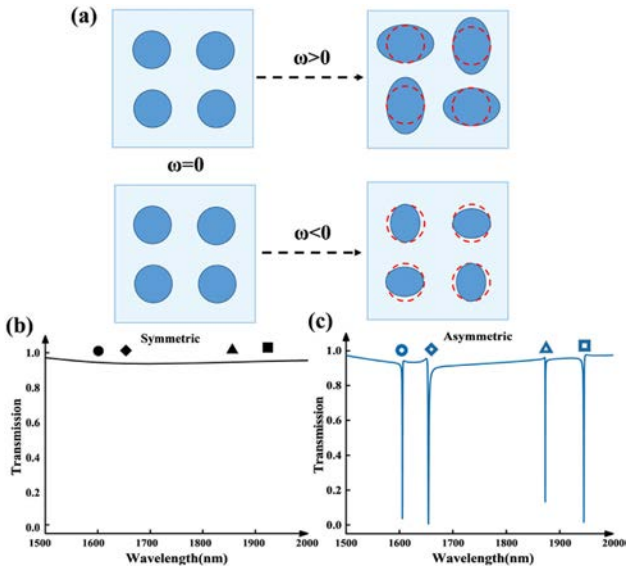

Fig. 2. (a) Destructive mechanics of the structural symmetry; (b) simulated spectra of the symmetric WETM; (c) the asymmetric WETM.

but different extension directions. The period of the unit cell $\mathbf{P}$ is 2000 nm, and the distance is $\mathbf{I} = 510$ nm from the center of the nanopillar in the x-direction to the central axis. The elliptical radius increment $\boldsymbol{\omega}$ is introduced as an asymmetry parameter to facilitate the adjustment of the tetramer shape. This parameter allows for controlled variation of the elliptical deformation, providing a convenient means to modify the geometry of the tetramer unit cells in the metasurface design. The Floquet-periodic boundary conditions are applied in the x- and y-directions, and the perfectly matched layer is located in the z-direction to absorb the reflected wave energy. The incident light is linearly polarized along the x-axis and propagates parallel to the z-axis, as shown in Fig. 1(c).

In order to illustrate the symmetry-breaking mechanism, the top view of the meta-unit is depicted in Fig. 2(a). Figures 2(b) and 2(c) present the calculated spectra of the symmetric WETM and asymmetric WETM at normal incidence. When WETM is symmetrical ($\boldsymbol{\omega} = 0$), there are no observable resonance modes. However, when the tetramer is asymmetrical ($\boldsymbol{\omega} \neq 0$), four

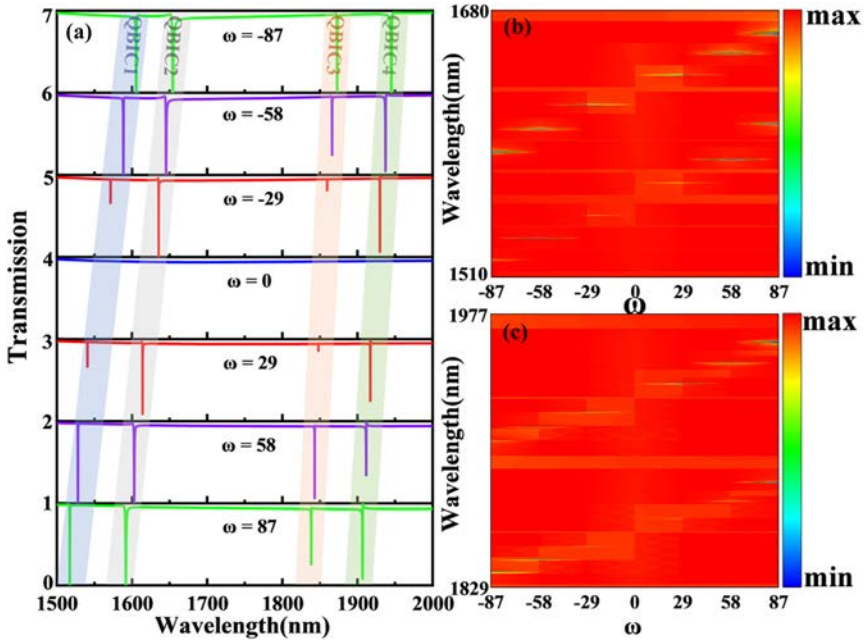

Fig. 3. (a) Transmission spectra of the metasurface showing the impact of different $\boldsymbol{\omega}$; (b) transmission mapping of QBIC1 and QBIC2 versus $\boldsymbol{\omega}$ and wavelength; (c) transmission mapping of QBIC3 and QBIC4 versus $\boldsymbol{\omega}$ and wavelength.

resonances are excited. The QBIC modes are generated at 1553, 1608, 1855, and 1928 nm. When the WETM with $\boldsymbol{\omega} = 0$ nm [i.e., no asymmetry, as shown in Fig. 2(b)] is introduced, the structure is perfectly symmetrical. In this case, no transmission dip is observed in the transmission spectrum, as the symmetry suppresses any phase mismatching or interference effects that can produce such dips. Specifically, the symmetry preserves the continuity of the optical field across the structure, thus preventing radiation leakage and avoiding the formation of resonant states that would otherwise manifest as transmission dips. As the degree of asymmetry increases [e.g., when $\boldsymbol{\omega} = 87$ nm, as shown in Fig. 2(c)], radiation leakage is observed due to symmetry breaking. The asymmetry leads to multiple QBIC modes, each characterized by a high-quality factor and suppressed radiation loss. These QBIC modes appear as distinct resonances in the transmission spectrum arising from the coupling of the local resonant modes to the continuum.

To evaluate the influence of symmetry and asymmetry on the transmission spectra, the transmission spectra of metasurfaces with different elliptical radius increments $\boldsymbol{\omega}$ from −87 to 87 nm are derived, as shown in Fig. 3(a). Results similar to Fig. 2(b) are obtained with $\boldsymbol{\omega} = 0$. In the asymmetrical structure, the four resonances are QBIC1, QBIC2, QBIC3, and QBIC4. As shown in Fig. 3(a), as $\boldsymbol{\omega}$ increases from −87 to 87 nm, all four resonances red shift, with QBIC1 showing the highest red shift frequency, followed by QBIC2, QBIC3, and QBIC4. Figures 3(b) and 3(c) show that the larger the $\boldsymbol{\omega}$ deviation from 0, the wider the FWHM of the transmission and the lower the Q value.

The Q-factor is defined as $Q = \frac{\lambda}{\mathrm{FWHM}}$, where λ is the resonant wavelength, and FWHM is the full-width at half-maximum of the resonance. In reality, the total Q-factor (Q_{total}) of the QBIC for radiation and dissipation is defined as

$$\frac{1}{Q_{\mathrm{total}}} = \frac{1}{Q_{\mathrm{radiation}}} + \frac{1}{Q_{\mathrm{dissipation}}}, \tag{1}$$

where $Q_{\mathrm{radiation}}$ and $Q_{\mathrm{dissipation}}$ correspond to the radiation and dissipation components of the Q-factor, respectively. The frequency and Q-factor of Fano resonance can be obtained by fitting the transmittance curve T using the classical Fano model, as demonstrated in recent studies exploring plasmonic systems where high-Q Fano resonances are triggered through asymmetry [27,28] and in precision-controlled symmetry-breaking methods for QBICs, which achieved ultrahigh-Q resonators [29]:

$$T(\omega) = T_0 + G\frac{\left[q + \frac{2(\omega-\omega_0)}{\tau}\right]^2}{1 + \left[\frac{2(\omega-\omega_0)}{\tau}\right]^2}. \tag{2}$$

In order to unveil the far-field radiation mechanism of the metasurface, multipole moments and their contributions to Fano resonances are determined by multipole decomposition in the Cartesian coordinate. By integrating the current density in the unit cell of the metasurface, the multipole moments can be defined as follows [30,31]:

Electric dipole moment:

$$\vec{P} = \frac{1}{i\omega}\int \vec{J}\,\mathrm{d}^3 r, \tag{3}$$

Magnetic dipole moment:

$$\vec{M} = \frac{1}{2C}\int (\vec{r}\times\vec{J})\mathrm{d}^3 r, \tag{4}$$

Toroidal dipole moment:

$$\vec{T} = \frac{1}{10C}\int \left[(\vec{r}\cdot\vec{J})\vec{r} - 2r^2\vec{J}\right]\mathrm{d}^3 r, \tag{5}$$

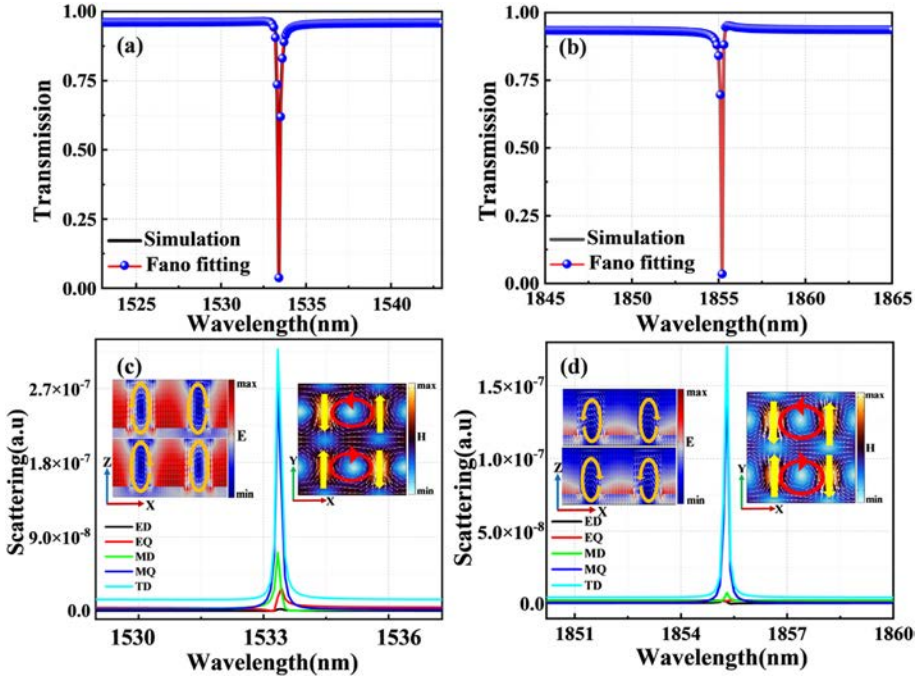

Fig. 4. (a) QBIC1 and (c) QBIC3 fitted results obtained by the Fano mode; multipolar decompositions of (b) QBIC1 and (d) QBIC3 with electric field distributions in the x-z plane and magnetic field distributions in the x-y plane.

Electric quadrupole moment:

$$Q_{\alpha\beta}^{(e)} = \frac{1}{2i\omega}\int\left[r_\alpha j_\beta + r_\beta j_\alpha - \frac{2}{3}(\vec{r}\cdot\vec{J})\delta_{\alpha,\beta}\right]\mathrm{d}^3 r, \quad (6)$$

Magnetic quadrupole moment:

$$Q_{\alpha\beta}^{(e)} = \frac{1}{3c}\int\left[(\vec{r}\times\vec{J})_\alpha j_\beta + \left((\vec{r}\cdot\vec{J})_\beta r_{\alpha,}\right]\mathrm{d}^3 r\ , \quad (7)$$

where c is the speed of light, $\boldsymbol{\omega}$ is the angular frequency of light, and $\alpha, \beta = x, y, z$. $\vec{j}$ is the current density distribution within a unit cell:

$$\vec{J} = -i\omega\varepsilon_0(n^2-1)\vec{E}. \quad (8)$$

In the near-infrared region, the curve fitting of QBIC1 and QBIC3 is presented in Figs. 4(a) and 4(b). The prediction of both resonances (black curve) for $\boldsymbol{\omega} = -58$ nm agrees with the simulation results (red and blue dotted lines) around the resonance dip, indicative of Fano resonance. To elucidate the origin of the resonances, the scattered power of multipole components is determined. When light waves pass through a medium, different scattering sources may produce multipole scattering effects, and various electromagnetic modes can couple with each other. This coupling effect produces interactions between different modes and interferences. Destructive interference occurs when the phase difference between multiple scattering sources or modes aligns, causing a significant attenuation of transmitted light intensity at specific frequencies or wavelengths. This phenomenon is typically observed as a dip in the transmitted light spectrum. Therefore, this dip reveals the interference effect caused by multipolar scattering and mode coupling. The total scattering efficiency of two resonant multipoles is mainly dominated by TD, followed by MQ, as shown in Figs. 4(c) and 4(b), respectively. The electric field of QBIC1 and QBIC3 comes from the four longitudinal electric resonances, in which the electric field is distributed on the outside and between the gaps of the tetramer and surrounds the center of each column to form a circular displacement current in the x-z plane (as indicated by the orange circular arrow). The x-y magnetic field direction is opposite, together forming a closed magnetic ring around the x-axis (as indicated by the bold red circular arrow), indicating the existence of TD. Meanwhile, the reverse structure of the magnetic field suggests the existence of MQ.

Figures 5(a) and 5(b) present the Fano fitting result for QBIC2 and QBIC4. In addition, Figs. 5(c) and 5(d) show that the contribution of TD dominates QBIC2 resonance. Obviously, the TD contribution dominates the response, followed by MQ. The electric and magnetic field distributions of QBIC2 and QBIC4 are shown in Figs. 5(c) and 5(d). The electric field is weaker in the nanodiscs and stronger in the outer part of the nanodiscs. Two sets of counterclockwise and clockwise closed displacement current loops are obtained on the x-y plane, respectively. On the x-z plane, the magnetic field vector direction on the cross-section of the nanocolumn is opposite, and this reverse distribution shows symmetry in multiple quadrants, indicating the existence of MQ. In addition, the directional arrows of the magnetic field vectors head-to-head form a loop and circulate clockwise along the z-direction, which is a characteristic of TD. Previous research reveals that TD resonance can be excited by constructing an elementary surface structure of tetramer clusters, and our structural model confirms it.

3. GEOMETRIC STRUCTURE DEPENDENCE

Since different sizes of the metasurface structure affect the properties, the linewidths, resonant frequencies, and transmission depths of the four resonances vary individually by adjusting

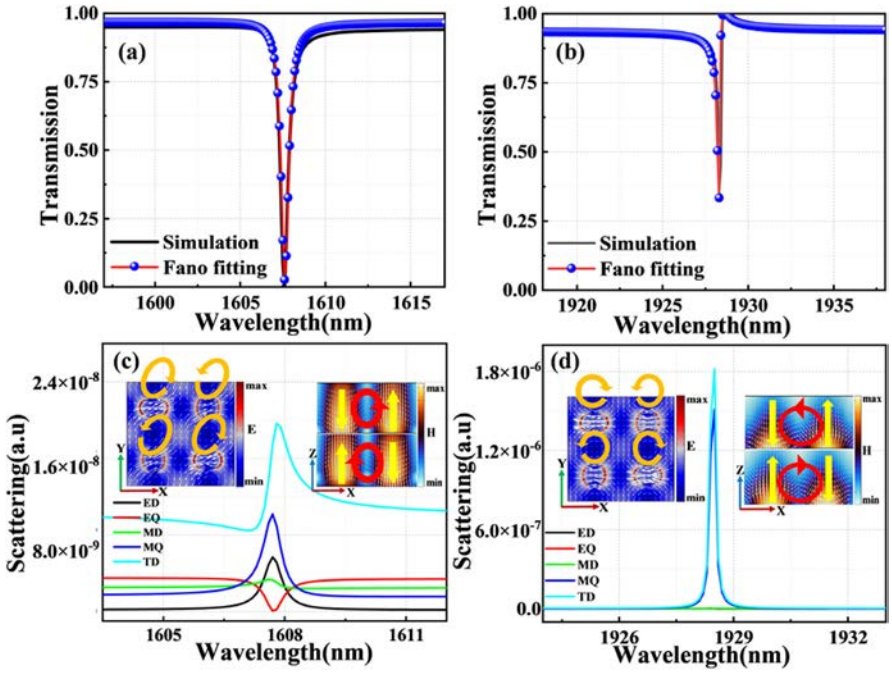

Fig. 5. (a) QBIC2 and (c) QBIC4 fitted results obtained by the Fano mode; multipolar decompositions of (b) QBIC2 and (d) QBIC4 with electric field distributions in the x-y plane and magnetic field distributions in the x-z plane.

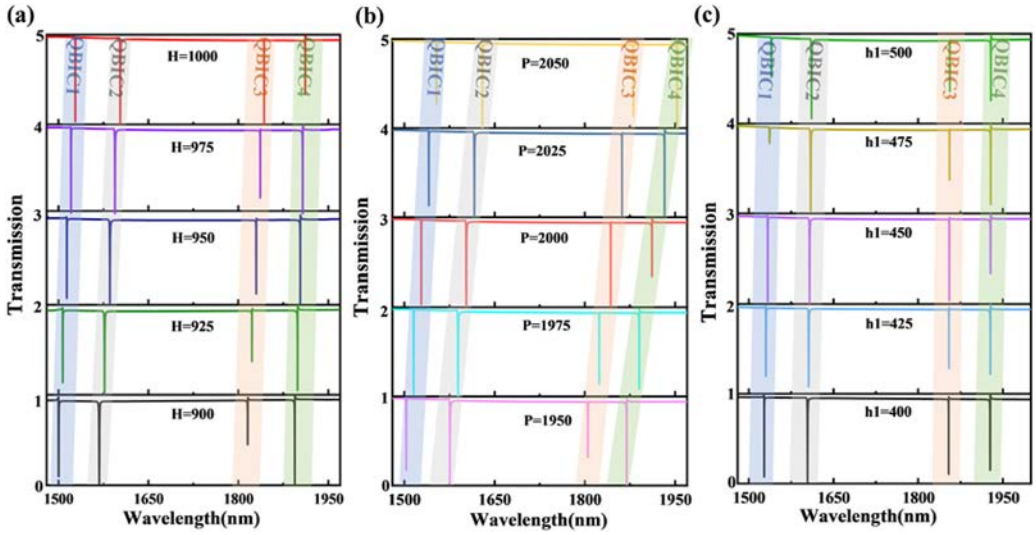

Fig. 6. Transmission spectra of the asymmetric metasurface structure ($\boldsymbol{\omega} = -58$ nm): (a) substrate thickness **H**, (b) period **P**, and (c) nanopillar height **h1**.

geometrical parameters such as **P**, **H**, and **h1**. For the purpose of illustration, the following geometric parameters are chosen: $\mathbf{P} = 2025$ nm, $\mathbf{H} = 975$ nm, $\mathbf{h1} = 450$ nm, $\mathbf{I} = 510$ nm, and $\mathbf{r} = 250$. To study the dependence on the different geometric parameters, the transmission spectra are calculated for the asymmetry parameter $\boldsymbol{\omega} = -58$ nm. The remaining geometric parameters are the same, except for the varying parameter shown in each figure. Figure 6(a) shows the optimization process for the different substrate thicknesses **H**. The four resonances, QBIC1, QBIC2, QBIC3, and QBIC4, red shift as **H** increases from 900 to 1000 nm. However, when **H** is changed in 20 nm increments, the shift of QBIC4 is less pronounced than that of the other three resonances. The four resonances show significant red shifts when **P** increases from 1950 to 2050 nm, as shown in Fig. 6(b). Finally, the impact of the nanopillar height (**h1**) on the transmission spectra is presented in Fig. 6(c). As **h1** gradually increases from 400 to 500 nm in steps of 25 nm, a small red shift of the transmission dip is observed.

The transmission valleys of the four modes red shift with increasing **H** and **P** because the volume of SiO_2 increases, and light undergoes more scattering in SiO_2, reducing the refractive index difference between SiO_2 and $LiNbO_3$. At the same time, more photon energy leaks from the $LiNbO_3$ layer into the SiO_2 layer, and the refractive indices of QBIC1, QBIC2, QBIC3,

and QBIC4 decrease, and the phase velocities increase. Hence, the four resonances move in the long-wavelength direction. In addition, the increase in the $LiNbO_3$ height promotes energy coupling between the modes, and the four resonances red shift, being consistent with **H** and **P**. Additionally, the thickness and size of the substrate affect the metasurface's overall optical properties and the interaction between surface plasmon polaritons and transmitted light, which is more likely to cause a larger red shift in the transmission dip [32]. In contrast, variations in the dielectric material height **h1** primarily influence the local modes, resulting in a smaller impact on the transmission dip [33].

4. POLARIZATION CHARACTERISTICS OF FOUR-BAND QBIC

The polarization angle ($\boldsymbol{\theta}^\circ$) is defined as the angle between the polarization orientation of a linearly polarized plane wave and the x-axis in the Cartesian coordinate system. A plane wave is utilized as the structural light source; the incident near-infrared light beam is polarized along the x-axis and propagates perpendicularly along the negative z-axis. Following our numerical analysis, we conducted polarization-dependent measurements. We selected a metasurface with a geometry of $\mathbf{H} = 975$ nm, $\mathbf{P} = 2025$ nm, and $\mathbf{h1} = 450$ nm, corresponding to the $\mathbf{h1} = 450$ nm curve in Fig. 6(c). Considering the difficulties of beam calibration and defects in manufacturing, the transmission spectra are determined for eight other polarization states (15° polarization, 30° polarization, 45° polarization, 60° polarization, 75° polarization, y-polarization, and left-handed and right-handed circular polarization), as shown in Fig. 7. Surprisingly, the transmission spectra for different polarization angles do not change, with QBIC1, QBIC2, and QBIC3 maintaining large amplitudes in different polarization directions, implying that WETM is polarization independent. In the metasurface design, we introduce structural perturbations to excite the QBIC resonance modes, while strictly preserving C_{4v} symmetry in both geometry and material distribution of the structure. Notably, these perturbations do not disrupt the C_{4v} symmetry but rather trigger specific resonant modes within the symmetry framework, potentially leading to polarization-independent transmission responses. For instance, Yang *et al.* [34] successfully achieved polarization-independent properties by designing the metasurface geometry to eliminate polarization-dependent propagation through symmetry design, showing the scalability and efficiency of dielectric particle-based metasurfaces for light localization and sensing. Additionally, Hsu *et al.* [35] pointed out that when the structure maintains high symmetry, modes from different symmetry classes decouple, preventing their coupling and effectively suppressing polarization effects. This is further corroborated by studies like those of Wang *et al.* [36], who demonstrated polarization-independent responses by selecting appropriate unit cells within a C_{4v}-symmetric structure and tuning parameters such as the size and position of the nanoholes, and Wang *et al.* [37] explored polarization-independent trapped modes (BICs) achieved by symmetry-breaking in dielectric resonators. These findings suggest that maintaining C_{4v} symmetry not only enhances the stability of the resonances but also enables

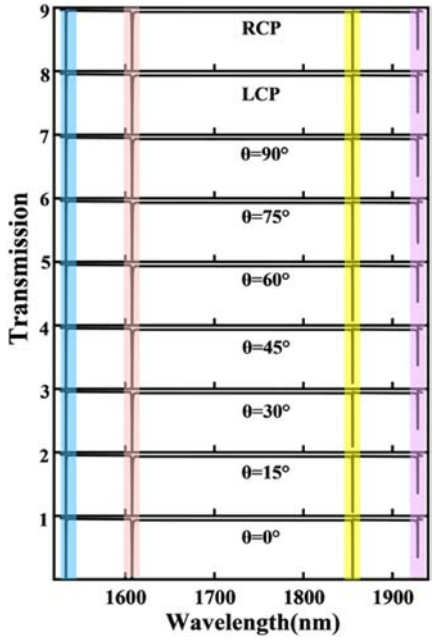

Fig. 7. Transmission spectra for different polarization angle $\boldsymbol{\theta}^\circ$.

polarization-independent light propagation, ensuring consistent transmission performance under varying polarization conditions [38,39].

This unique characteristic can be exploited to eliminate or even significantly reduce the need for polarization calibration, thus providing greater flexibility for applications such as projectors, radar technology, microscope systems, and solar cells.

5. SENSING CHARACTERISTICS OF FOUR-BAND QBIC

For ultra-sensitive sensors, an ultra-high Q factor and strong field enhancement are crucial in order to detect subtle changes in the gas environment, which produce frequency shifts in gas sensing [30,31,40,41] or refractive index sensing [30]. The high Q factor in multiple resonance modes makes the metasurface promising, and the sensing properties of the WETM are determined. The QBIC for an $\boldsymbol{\omega} = -58$ nm metasurface is demonstrated by exciting with an x-polarized plane wave and changing the refractive index of the environment from $\mathbf{n} = 1.001$ to $\mathbf{n} = 1.01$. Equal-interval red shifts are observed with changing environmental RIs for the four resonances, as shown in Fig. 8. Increasing the refractive index of the gas from 1.001 to 1.01 produces red shifts for all four resonance wavelengths.

To evaluate the sensing performance, the sensitivity (S) and figure of merit (FOM) are derived. The sensitivity (S) is defined in Eq. (9) [5], and the figure of merit (FOM) in Eq. (10) [42]:

$$S = \frac{\Delta\lambda}{\Delta n}\ (\text{nm/RIU}), \tag{9}$$

where Δn is the RI change, and $\Delta\lambda$ is the shift of the center wavelength with Δn. The FOM [43] incorporates the S and Q factors and is adopted to assess the comprehensive resolving

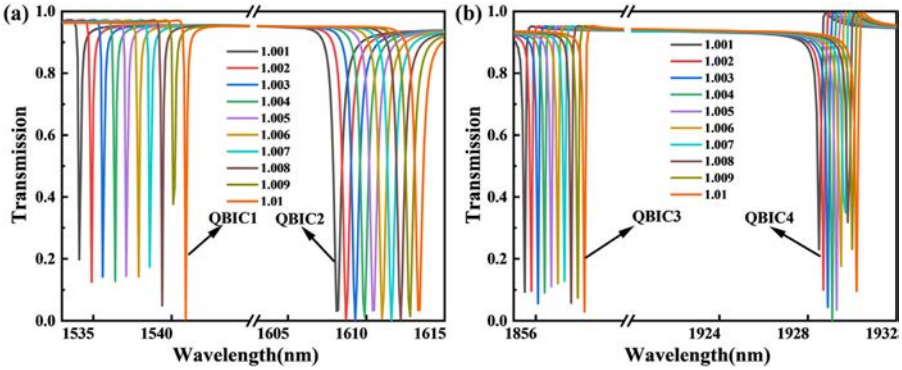

Fig. 8. Transmission spectra for refractive indexes going up from 1.0001 to 1.0009: (a) QBIC1 and QBIC2; (b) QBIC3 and QBIC4.

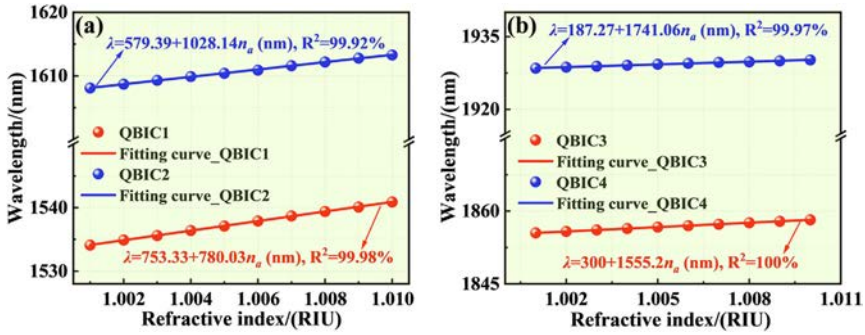

Fig. 9. (a) Linear fitting of QBIC1, QBIC2, and refractive index; (b) linear fitting of QBIC3, QBIC4, and refractive index.

power of an optical sensor. It is defined as

$$\mathrm{FOM} = \frac{S}{\mathrm{FWHM}}(\mathrm{RIU}^{-1}). \tag{10}$$

To measure the sensitivity of the WETM, linear fitting is applied to the wavelength positions of the four resonances for different refractive indexes, as shown in Figs. 9(a) and 9(b). The linear fitting expressions in the figure show R^2 greater than 99.9%. The fitting results reveal that the sensitivities of QBIC1, QBIC2, QBIC3, and QBIC4 are 753.33, 579.39, 300, and 187.27 nm/RIU, respectively, and the corresponding FOMs are 5707, 1089, 3409, and 918 RIU^{-1}.

6. CONCLUSION

A C_{4v} all-dielectric metasurface with four BICs is designed and investigated. The metasurface consists of four elliptic tetramer metasurfaces with four $LiNbO_3$ ellipsoidal columns arranged on an SiO_2 substrate. It exhibits significant sharp Fano resonance near 1553, 1608, 1855, and 1928 nm and Q factors of 1.15×10^4, 0.302×10^4, 2.1×10^4, and 0.94×10^4, respectively. The four modes are selected to yield very high sensitivity and FOMs. The electric field and magnetic field distributions and multipole scattering power are derived to confirm the excitation of TD and MQ at the resonance wavelength. Furthermore, different combinations of asymmetry and structural parameters are investigated. The results show that polarization independence can be steadily excited in these structures. Overall, the QBICs-based all-dielectric metasurface delivers high performance in nanoparticle detection and has great potential in applications such as refractive index detection and gas sensing.

APPENDIX A: FEASIBLE PRODUCTION PROCESS

The manufacturing process of the WETM is discussed. Figure 10 shows the manufacturing steps for the metasurface. Prior to fabrication, acetone is used to remove organic contaminants, followed by cleaning with isopropyl alcohol (IPA) and thorough rinsing with deionized water to remove oil, dust, and other contaminants from the melted SiO_2 surface. After cleaning, an $LiNbO_3$ film is deposited onto the SiO_2 substrate by low-pressure chemical vapor deposition (LPCVD). The poor conductivity of the SiO_2 substrate is mitigated by coating the $LiNbO_3$ film with ZEP520 photoresist and AR-PC conductive glue. Subsequently, the metasurface patterns

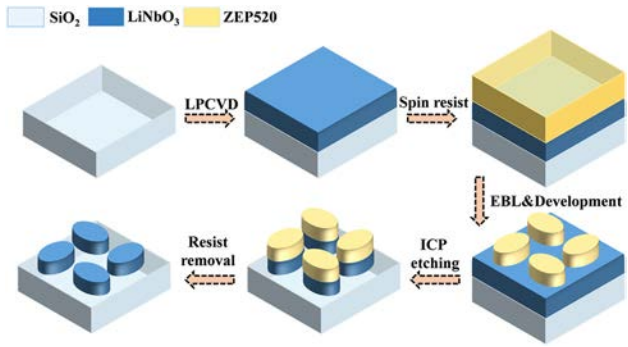

Fig. 10. Manufacturing process of the WETM.

are defined using photoresist by electron-beam lithography (EBL). After development, fixation, and etching, the sample is immersed in acetone to remove the adhesive. Finally, the sample is rinsed with deionized water and dried with nitrogen to ensure no watermarks remain.

Funding. National Natural Science Foundation of China (12304480); Heilongjiang Provincial Natural Science Foundation of China (JQ2023F001); Natural Science Foundation of Heilongjiang Province LH2021F007; City University of Hong Kong Donation Research Grants (9229021, 9220061).

Disclosures. The authors declare no conflicts of interest.

Data availability. Data underlying the results presented in this paper are not publicly available at this time but may be obtained from the authors upon reasonable request.

REFERENCES

1. V. Pistore, L. Viti, C. Schiattarella, *et al.*, "Terahertz plasmon polaritons in large area Bi2Se3 topological insulators," Adv. Opt. Mater. **12**, 2301673 (2024).
2. M. Huang, B. Zheng, R. Li, *et al.*, "Evolutionary games-assisted synchronization metasurface for simultaneous multisource invisibility cloaking," Adv. Funct. Mater. **34**, 2401909 (2024).
3. Q. H. Lv, X. Qin, M. Z. Hu, *et al.*, "Metatronics-inspired high-selectivity metasurface filter," Nanophotonics **13**, 2995–3003 (2024).
4. S. L. Xian, S. S. Huang, K. H. Qiu, *et al.*, "Highly precise and broadband full-stokes polarimeter based on a deep learning algorithm," ACS Photonics **10** 2432–2439 (2023).
5. J. X. Wang, X. L. Lu, C. Mi, *et al.*, "Ultra-high sensitivity photonic crystal fiber sensor based on dispersion turning point sensitization of surface plasmonic polariton modes for low RI liquid detection," Opt. Express **32**, 32895–32908 (2024).
6. N. Muhammad, A. Begum, Z. Su, *et al.*, "Second harmonic generation from bound-state in the continuum-hosted few-layers van der Waals metasurface," Nanophotonics **14**, 263–270 (2025).
7. Y. Ren, J. W. Lv, C. Liu, *et al.*, "Dual modulation polarization-independent terahertz bic metasurface for multi-wavelength sensing," Coatings **15**, 363 (2025).
8. K. Watanabe, T. Nagao, and M. Iwanaga, "Low-contrast BIC metasurfaces with quality factors exceeding 100,000," Nano Lett. **25**, 2777–2784 (2025).
9. W. J. Shi, Z. L. Wang, J. C. Liu, *et al.*, "Enhanced the tunable nonlinearity of epsilon-near-zero nonlocal metasurface by quasi-guided mode," Laser Photonics Rev. **19**, 2402312 (2025).
10. Y. Sun, C. He, Z. Deng, *et al.*, "Optical chirality of all dielectric q-BIC metasurface with symmetry breaking," Nanophotonics **14**, 559–569 (2025).
11. O. A. M. Abdelraouf, M. Wu, and H. Liu, "Hybrid metasurfaces enabling focused tunable amplified photoluminescence through dual bound states in the continuum," Adv. Funct. Mater. 2505165 (2025).
12. S. Eyvazi, E. A. Mamonov, R. Heilmann, *et al.*, "Flat-band lasing in silicon waveguide-integrated metasurfaces," ACS Photonics **12**, 1570–1578 (2025).
13. C. Chen, P. Gao, Y. W. Dai, *et al.*, "All-dielectric near-infrared metasurface with field enhancement and high Q-factor based on anapole precise manipulation," Adv. Opt. Mater. **13**, 2403312 (2025).
14. N. Shitrit, "Surface-emitting lasers meet metasurfaces," Light Sci. Appl. **13**, 37 (2024).
15. H. Li, W. Yu, M. Pan, *et al.*, "Multi-degree-of-freedom stretchable metasurface terahertz sensor for trace cinnamoylglycine detection," Biosensors **14**, 602 (2024).
16. S. Karepov, C. De Angelis, and T. Ellenbogen, "Hybrid nonlinear metasurface refractive lens," Nano Lett. **25**, 8103–8109 (2025).
17. H. Hu, W. Lu, A. Antonov, *et al.*, "Environmental permittivity-asymmetric BIC metasurfaces with electrical reconfigurability," Nat. Commun. **15**, 7050 (2024).
18. Z. Xie, C. Li, K. Murali, *et al.*, "Ultrathin BIC metasurfaces based on ultra-low-loss Sb2Se3 phase-change material," Nano Lett. **25**, 251–260 (2024).
19. J. Deng, Z. Hu, Y. Chen, *et al.*, "Nonlinear optical information encoding with grayscale lithography enabled metasurfaces," Nano Lett. **25**, 7450–7456 (2025).
20. P. N. Li, G. W. Hu, I. Dolado, *et al.*, "Collective near-field coupling and nonlocal phenomena in infrared-phononic metasurfaces for nano-light canalization," Nat. Commun. **11**, 3663 (2020).
21. H. Wu, X. X. Gao, L. Zhang, *et al.*, "Harmonic information transitions of spatiotemporal metasurfaces," Light Sci. Appl. **9**, 198 (2020).
22. Z. Xi and Z. Chen, "Conversion and active control between BIC and absorber in terahertz metasurface," Photonics **11**, 437 (2024).
23. Y. Fan, B. Li, L. Zeng, *et al.*, "Dual-quasi BIC enabled plasmonic metasurfaces and active switch between BIC and quasi-BIC," Phys. Scr. **100**, 055905 (2025).
24. B. Gao, M. X. Ren, W. Wu, *et al.*, "Lithium niobate metasurfaces," Laser Photonics Rev. **13**, 1800312 (2019).
25. R. Kanyang, C. Z. Fang, Y. B. Wang, *et al.*, "Tunable lithium niobate metasurfaces for phase-only modulation based on quasi-bound states in the continuum," Sci. China Inf. Sci. **67**, 219401 (2024).
26. W. C. He and Y. S. Wang, "Enhancement of second-harmonic generation in a lithium niobate metasurface by exploring the bound states in the continuum," Opt. Express **32**, 39415–39428 (2024).
27. C. B. Zhou, S. Y. Li, Y. Wang, *et al.*, "Multiple toroidal dipole Fano resonances of asymmetric dielectric nanohole arrays," Phys. Rev. B **100**, 195306 (2019).
28. W. X. Lim, M. Manjappa, P. Pitchappa, *et al.*, "Shaping high-Q planar Fano resonant metamaterials toward futuristic technologies," Adv. Opt. Mater. **6**, 1800502 (2018).
29. C. Zhou, M. Zhou, Z. Fu, *et al.*, "Ultrahigh-*Q* quasi-BICs via precision-controlled asymmetry in dielectric metasurfaces," Nano Lett. **25**, 5916–5924 (2025).
30. Z. Q. Liu, B. Wang, S. Wang, *et al.*, "Mid-infrared high performance dual-Fano resonances based on all-dielectric metasurface for refractive index and gas sensing," Opt. Laser Technol. **177**, 111140 (2024).
31. J. Wang, H. Zhang, S. Chen, *et al.*, "A silicon microring resonator for refractive index carbon dioxide gas sensing," ACS Sens. **10**, 4938–4944 (2025).
32. Q. S. Wei, L. L. Huang, T. Zentgraf, *et al.*, "Optical wavefront shaping based on functional metasurfaces," Nanophotonics **9**, 987–1002 (2020).
33. W. W. Liu, Z. C. Li, H. Cheng, *et al.*, "Dielectric resonance-based optical metasurfaces: from fundamentals to applications," iScience **23**, 2589-0042 (2020).
34. X. Y. Yang, A. Antonov, A. Aigner, *et al.*, "Polarization-independent metasurfaces based on bound states in the continuum with high Q-factor and resonance modulation," Opt. Express **33**, 15682–15689 (2025).
35. C. W. Hsu, B. Zhen, A. D. Stone, *et al.*, "Bound states in the continuum," Nat. Rev. Mater. **1**, 1–13 (2016).
36. X. Wang, S. Li, and C. Zhou, "Polarization-independent toroidal dipole resonances driven by symmetry-protected BIC in ultraviolet region," Opt. Express **28**, 11983–11989 (2020).
37. L. L. Wang, C. B. Zhou, Y. Zhang, *et al.*, "Polarization-Independent high *Q*-factor resonance achieved by efficiently selecting and perturbing the unit cell of nanostructure," J. Lightwave Technol. **43**, 757–763 (2025).
38. P. Vaity, H. Gupta, A. Kala, *et al.*, "Polarization-independent quasi-bound states in the continuum," Adv. Photonics Res. **3**, 2100144 (2022).
39. A. Sayanskiy, A. S. Kupriianov, S. Xu, *et al.*, "Controlling high-*Q* trapped modes in polarization-insensitive all-dielectric metasurfaces," Phys. Rev. B **99**, 085306 (2019).
40. P. C. Wu, C. Y. Liao, V. Savinov, *et al.*, "Optical anapole metamaterial," ACS Nano **12**, 1920–1927 (2018).
41. T. T. Treena, N. M. Munim, M. R. Islam, *et al.*, "Comparative analysis of elliptical cavities for refractive index sensing for biomedical and industrial gas detection applications," Opt. Laser Technol. **181**, 111805 (2025).

42. C. Liu, J. Wang, J. Lv, *et al.*, "Economical and easily implemented Vernier effect bubble microcavity FPI for strain sensing with extreme low-temperature cross-sensitivity," Infrared Phys. Technol. **150**, 105939 (2025).

43. H. Fu, Y. Guo, W. Gao, *et al.*, "Ultra-high sensitivity weak magnetic field detecting magnetic fluid surface plasmon resonance sensor based on a single-hole fiber," Opt. Express **32**, 15025–15040 (2024).